RSC Advances

ROYAL SOCIETY OF CHEMISTRY

www.rsc.org/advances

Journal Name

ARTICLE

Effect of iron doping on the photocatalytic activity of Bi_2WO_6-$BiVO_4$ composite

Received 00th January 20xx,
Accepted 00th January 20xx

DOI: 10.1039/x0xx00000x

www.rsc.org/

Saranyoo Chaiwichian[a], Khatcharin Wetchakun[b], Sukon Phanichphant[c], Wiyong Kangwansupamonkon[d], Natda Wetchakun[a*]

The visible-light-driven Fe-doped Bi_2WO_6-$BiVO_4$ composites have been synthesized via a hydrothermal method with varying nominal iron contents in the range of 0.5–5.0 mol%. The physicochemical properties of the obtained materials were characterized by X-ray diffraction (XRD), Brunauer-Emmett-Teller (BET)-specific surface area, transmission electron microscopy (TEM), X-ray photoelectron spectroscopy (XPS), inductively coupled plasma-optical emission spectroscopy (ICP-OES), UV-vis diffuse reflectance spectroscopy (UV-vis DRS), and photoluminescence (PL) techniques. Methylene blue (MB) as probe pollutant was adopted to investigate the photocatalytic activity of all samples under visible light irradiation. The Fe-doped Bi_2WO_6-$BiVO_4$ composites showed an enhanced photocatalytic activity for the degradation of MB under visible light, which was attributed to iron ion acting as a good electron and hole traps for facilitating in separation of charge carriers. Simultaneously, high stability of the sample was also investigated by five times of successive photodegradation testing of MB under visible light. The relationship between photocatalytic activities and the structures of Fe-doped Bi_2WO_6-$BiVO_4$ composites were discussed. The possible photocatalytic mechanism of the composites was proposed to guide the further improvement of their photocatalytic performance.

1 Introduction

Semiconductor-based photocatalysis has been receiving a great deal of attention due to its prominent ability in eliminating harmful organic pollutants in water.[1,2] The key to enhance the photocatalytic activity of semiconductor mainly lies in effectively combining photon absorption, bulk diffusion and separation of photoexcited electron-hole pairs.[3] In recent years, bismuth vanadate ($BiVO_4$) has been one of the most appealing candidates in the treatment of dye-containing wastewaters.[4] $BiVO_4$ have three main crystalline structures such as tetragonal scheelite, tetragonal zircon and monoclinic scheelite. The $BiVO_4$ has attracted in considerable interest for its good visible-light-induced photocatalytic property.[5-7] However, the low separation efficiency of photoinduced electrons and holes, limit wide application of $BiVO_4$ in the fields of environment remediation.[8,9] To resolve this problem, the composite photocatalysts comprised of two semiconducting oxides has been alternated to enhance the photocatalytic performance by improving the charge carrier separation.[10-12] Bismuth tungstate (Bi_2WO_6) has also attracted interest to be a promising visible-light-driven photocatalyst material owing to its good photocatalytic performance.[13,14] The production of a Bi_2WO_6/$BiVO_4$ composite is proposed as a way to reduce losses from electron-hole pair recombination, thereby improve photocatalytic performance. Moreover, an effective approach to increase photocatalytic efficiency of Bi_2WO_6-$BiVO_4$ composite is by doping it with transition metal ions such as Fe, Mo, Cu, Ni, Co and so on.[15,16] The enhancement of photocatalytic activity is achieved possibly due to the metals acting as electron and hole traps, so it promotes electron-hole separation and the interfacial charge-transfer process.[17-19] For in this work, iron (III) ion (Fe^{3+}) candidate was selected as a metal ion for trapping electron by doping to $BiVO_4$-Bi_2WO_6 composite. The fabrication of Fe-doped Bi_2WO_6-$BiVO_4$ composite is a challenging task in photocatalytic applications. To the best of our knowledge, investigations on the photocatalytic activity of Fe-doped Bi_2WO_6-$BiVO_4$ composite have not been attempted yet. This novel system was expected on band theory basis to its potential advantages, such as improvement of the tuneable light absorption, the photogenerated electron-hole separation, the interfacial charge transfer efficiency, and the oxidation ability.

In this study, we fabricated Fe-doped Bi_2WO_6-$BiVO_4$ composites by a hydrothermal method and characterized in detail. The different amounts of iron in Bi_2WO_6-$BiVO_4$ system were varied in the range of 0.5-5.0 mol%. The photocatalytic activity of all samples were examined by utilizing methylene blue (MB) as a target pollutant under visible-light irradiation ($\lambda > 400$ nm). Recycled stability test were evaluated for indicating that the presence of Fe-doped Bi_2WO_6-$BiVO_4$ composite contributes to photocorrosion inhibition for effectively applying photocatalytic activity. The possible photocatalytic mechanisms of Fe-doped Bi_2WO_6-$BiVO_4$ composite were proposed.

2 Experimental

2.1 Synthesis of the photocatalysts

2.1.1 Synthesis of bismuth tungstate (Bi_2WO_6)

Bi_2WO_6 particles were synthesized by using a hydrothermal method. Bismuth nitrate pentahydrate ($Bi(NO_3)_3{\cdot}5H_2O$) and sodium

[a] Department of Physics and Materials Science, Faculty of Science, Chiang Mai University, Chiang Mai 50200, Thailand.E-mail: natda_we@yahoo.com
[b] Program of Physics, Faculty of Science, Ubon Ratchathani Rajabhat University, Ubon Ratchathani 34000, Thailand.
[c] Materials Science Research Center, Faculty of Science, Chiang Mai University, Chiang Mai 50200, Thailand.
[d] National Nanotechnology Center, Thailand Science Park, Phahonyothin Road, Klong 1, Klong Luang, Phathumthani, 12120, Thailand.

tungstate dihydate ($Na_2WO_4{\cdot}2H_2O$) were used as precursors. Firstly, 0.008 M of $Bi(NO_3)_3{\cdot}5H_2O$ was dissolved in 2.5 M of nitric acid solution while 0.004 M of $Na_2WO_4{\cdot}2H_2O$ was dissolved in deionized water. The mixture of both solutions was kept under constant stirring until a homogeneous solution was obtained. Secondly, 6.0 M ammonium hydroxide (NH_4OH) was slowly added into the homogeneous solution until its pH equal to 7. The obtained solution was transferred into a teflon-lined stainless steel autoclave and then the hydrothermal reaction was carried out at 200°C for 24 h. Finally, the precipitates were washed with deionized water for several times and dried at temperature of 80°C for 24 h. The precipitates were finally collected by centrifugation and then washed 3 times with deionized water and dried at 80°C for 24 h.

2.1.2 Synthesis of Bi_2WO_6-$BiVO_4$ and 0.5-5.0 mol% Fe-doped Bi_2WO_6-$BiVO_4$ composites

The Bi_2WO_6-$BiVO_4$ composite was synthesized with 1:1 mole ratio of Bi_2WO_6:$BiVO_4$ by hydrothermal method. Firstly, 0.1 M of bismuth nitrate pentahydrate ($Bi(NO_3)_3{\cdot}5H_2O$) and 0.1 M of ammonium metavanadate (NH_4VO_3) was dissolved in 2.5 M of nitric acid. Secondly, 6.0 M of ammonium hydroxide was added dropwise into the solution for adjusting its pH to 4.5. Then, the completely prepared Bi_2WO_6 powders were added into the mixed solution in 1:1 of Bi_2WO_6:$BiVO_4$. After that, the suspension was transferred into a teflon-lined stainless steel autoclave and the hydrothermal reaction was carried out at 180°C for 6 h. Finally, Bi_2WO_6-$BiVO_4$ composite was obtained by filtrating and drying at 80 °C for 24 h. For controlling the experiment, pure $BiVO_4$ photocatalyst was also prepared with the same synthesis procedure but without adding Bi_2WO_6 particles.

To synthesize Fe-doped Bi_2WO_6-$BiVO_4$ composites, an amount of iron with different mole percentages of 0.5, 1.0, 2.0 and, 5.0 calculated from nitrate nonahydrate ($Fe(NO_3)_3{\cdot}9H_2O$) solution was added to the above solution of the prepared $BiVO_4$ in the same time with Bi_2WO_6 particles adding. The resulting suspension was then dispersed with ultrasonication bath. The obtained suspension was heated at temperature of 180°C for 6 h into a teflon-lined stainless steel autoclave. Finally, the precipitates were washed with deionized water for several times until pH equal to 7 and dried at temperature of 80°C for 24 h.

2.2 Sample characterization

The crystal structure of all samples were examined by X-ray diffraction (XRD, Philips X'Pert MPD) with Cu K_α irradiation (λ=1.5418 nm) in 2θ ranging from 20° to 60°. Transmission electron microscopy (TEM) images were taken using a JEOL JEM-2010 for investigating of their morphologies and d-spacing values. The Brunauer-Emmett-Teller (BET) method was employed to determine the surface area of the prepared samples by nitrogen absorption-desorption isotherm analysis at 80°C (Autosorb 1 MP, Quantachrom). X-ray photoelectron spectroscopy (XPS) was carried out on a Kratos Axis ULTRA "DLD" instrument equipped with a monochromatic source (Al K_α X-rays at 1.4 keV). The binding energy of the adventitious carbon (C 1s) line at 285 eV was used for calibration, and the positions of other peaks were corrected according to the position of the C 1s signal. Actual iron doping concentration was determined using inductively coupled plasma-optical emission spectroscopy (ICP-OES, Perkin-Elmer Optima 4300DV). UV-vis diffuse reflectance spectra of the prepared samples were collected on a UV-vis spectrometer (Perkin Elmer Lambda 1050) by using MgO as a reference and were converted from reflectance to absorbance by using Kubelka-Munk method. The photoluminescence (PL) technique was used to measure the emission properties of all samples using AvaSpec-2048TEC-USB2-2 spectrophotometer excited through LED (Oceans optics, LLS-345) as a light source at wavelength of 345 nm.

2.3 Photocatalytic activity experiments

Photocatalytic activities of all samples were examined by the degradation of methylene blue (MB) with the initial concentration of $2x10^{-5}$ M under visible light illumination. A 50 W halogen lamp (Essential MR, Philips (Thailand)), providing a light intensity of ~640 W m^{-2} was used as a visible light source filtered with a filter glass to remove UV range of the light (λ≤400 nm). In a typical run, 0.1 g of catalyst was were suspended in 100 mL of MB solution. The suspension was stirred in the dark for 24 h to obtain a good dispersion and establish adsorption-desorption equilibrium between the organic molecules and the catalyst surface. After illumination at each time of 0, 15, 30, 45, 60, 75, 90, 105 and 120 min, 5 mL of the solution was removed and immediately centrifuged to separate the solid. The clean transparent solution was analyzed using UV-vis spectrophotometer (Shimadzu UV-1800) recording the variations in the maximum absorption wavelength at 664 nm of MB. The photodegradation percentage of MB was calculated following the equation: $\%degradation=[(C_0-C_t)/C_0]\times100$, where C_0 is the initial concentration of MB after adsorption-desorption equilibrium and C_t is the concentration of MB at the specific testing time during the degradation.

2.4 Analysis of hydroxyl radical ($OH^\bullet$)

The formation of hydroxyl radical ($OH^\bullet$) on the surface of 2.0 mol% Fe-doped Bi_2WO_6-$BiVO_4$ composite which pass though photo-illumination was detected using photoluminescence (PL) technique composing of terephthalic acid as a probe molecule. Terephthalic acid (TA) readily reacts with $OH^\bullet$ to produce highly fluorescent product of 2-hydroxyterephthalic acid.[20] The intensity of the photoluminescence (PL) peak of 2-hydroxyterephtalic acid depends on the amount of $OH^\bullet$ radicals produced in water. The optimal concentrations were found 5×10^{-4} M of terephthalic acid solution and 2×10^{-3} M of a diluted sodium hydroxide (NaOH) aqueous solution. This method relies on the PL signal at 425 nm of the hydroxylation of terephthalic acid with $OH^\bullet$ generated in photocatalysis process. In a typical run, 0.1 g of 2.0 mol% Fe-doped Bi_2WO_6-$BiVO_4$ composite was dispersed into 100 mL of the TA solution mixture. The solution was collected every 30 min during visible light illumination in order to estimate the generated TA-$OH^\bullet$, analyzed by fluorescence spectroscopy at 425 nm.

3. Results and discussion

3.1 XRD and BET analyses

XRD pattern of all samples was shown in Fig. 1a. The crystal structure of $BiVO_4$ reveals to the monoclinic and tetragonal crystalline phases. The main monoclinic peaks were appeared at 2θ = 28.83°, 30.51°, 34.56°, 35.26°, 39.78°, 42.50°, 46.69°and 47.28° which corresponds to the ($\bar{1}$21), (040), (200), (002), (211), (051), (240) and (042) planes of $BiVO_4$ (JCPDS file No. 14-0688), respectively. The two strong diffraction peaks at 2θ of 24.37° and 32.69° are belonging to the (200) and (112) planes of tetragonal $BiVO_4$ which corresponds to JCPDS file no. 14-0133. The diffraction peaks of Bi_2WO_6 show the orthorhombic phase at 2θ of 28.47°, 32.89°, 47.29° and 55.93°, which can be indexed as the (113), (200), (220) and (313) planes corresponding to JCPDS files no. 73-1126.

The XRD pattern of the composites displays the diffraction peaks from both Bi_2WO_6 and $BiVO_4$ phases. No diffraction peaks from any other impurities are detected, confirming the high purity of this composite.

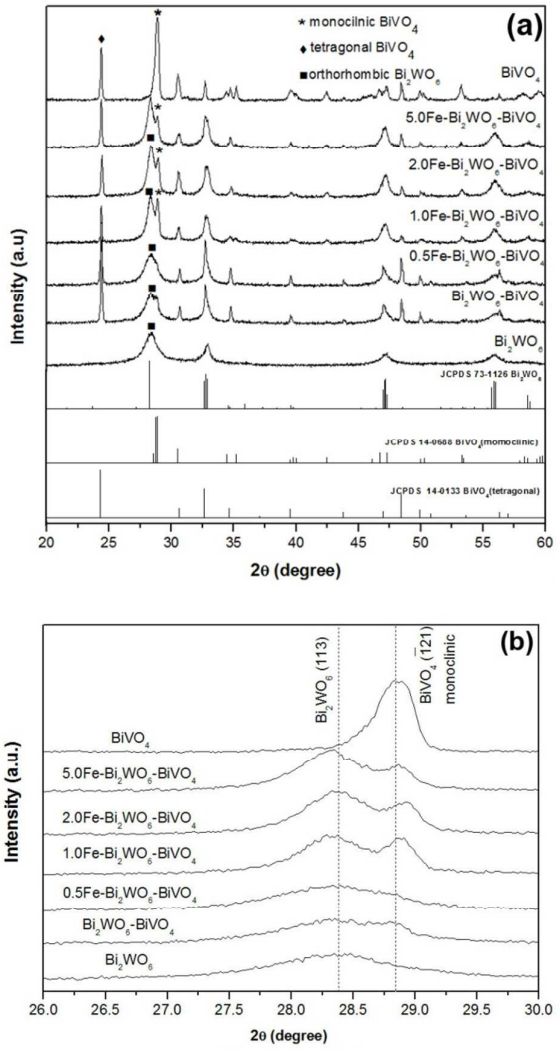

Fig. 1 XRD patterns of $BiVO_4$, Bi_2WO_6 and Fe-doped Bi_2WO_6-$BiVO_4$ with nominal iron contents of 0.5-5.0 mol% in the 2θ range (a) 20°-60° and (b) 26°-30°.

The XRD peak of Fe dopant was not detected, possibly because iron was doped in the range of very low concentration. Peak position of (113) and ($\bar{1}$21) planes of orthorhombic Bi_2WO_6 and monoclinic $BiVO_4$, respectively, shift upon doping with iron. This phenomenon indicates that the distortion of individual Bi_2WO_6 and $BiVO_4$ crystal lattice by iron dopant[18,19] as shown in Fig. 1b. The result was ascribed both $BiVO_4$ and Bi_2WO_6 lattice distortions to the substitution of bismuth ion with iron ion, corresponding to the ionic radius of Fe^{3+} (0.64 Å)[21] which was slightly smaller than that of Bi^{3+} (1.11 Å).[22] The observed shift in the (113) peak of Bi_2WO_6 to a lower 2θ values (larger d-spacing), possibly due to an expansion of the lattice in the Bi_2WO_6 unit cell. The lattice expansion in Bi_2WO_6-$BiVO_4$ composite and 0.5-5.0 mol% Fe-doped Bi_2WO_6-$BiVO_4$ composites could occur from 2-step heat treatment of Bi_2WO_6 according to the preparation method as described in section of "2.1 Synthesis of the photocatalysts". Moreover, the (113) peak of Bi_2WO_6 shift gradually to smaller angle with increasing iron dopant concentration. This implies that some Fe^{3+} ions could incorporate in Bi_2WO_6.

The values of specific surface area for $BiVO_4$, Bi_2WO_6, Bi_2WO_6/$BiVO_4$, and 2.0 mol% Fe-doped Bi_2WO_6-$BiVO_4$ samples were 13.6 $m^2 g^{-1}$, 44.0 $m^2 g^{-1}$, 22.0 $m^2 g^{-1}$, and 26.9 $m^2 g^{-1}$, respectively. The BET results show that doping of Bi_2WO_6/$BiVO_4$ composite with Fe ions, resulting in an increase of specific surface area. It was possibly due to Fe^{3+} substituted for Bi^{3+} in Bi_2WO_6 and $BiVO_4$ lattice. A large number of surface area with nanoparticles due to adsorption, desorption and diffusion of the reactants is favorable for improving photocatalytic activity.[23] However, the enhancement of photocatalytic activity is related to various factors such as type of catalyst, crystal structure, morphology, pH, light intensity, and so on which is not only for the surface area alone.

3.2 TEM analysis

Pure $BiVO_4$ (Fig. 2a) presents rod-like structure with sizes in the range of 50-80 nm in width and 100-200 nm in length. The d-spacing of 0.3083 nm is in good agreement with the ($\bar{1}$21) plane of $BiVO_4$ as shown in Fig. 2b. The morphology of pure Bi_2WO_6 (Fig. 2c) shows plate-like shape with size approximately 100 nm in both edges of its shape. The fringe spacing of 0.2729 nm and 0.4109 nm corresponds to the (200) and (040) planes of Bi_2WO_6 (Fig. 2d). The morphology of Bi_2WO_6-$BiVO_4$ sample consists of rod-like and plate-like structures as shown in Fig. 2e. The fringe spacing of 0.2926 nm matches with (040) plane of $BiVO_4$, while the plane of Bi_2WO_6 was not observed as shown in Fig. 2f. The TEM images of 2.0 mol% Fe-doped Bi_2WO_6-$BiVO_4$ composite are similar to rod- and plate-like structures of $BiVO_4$ and Bi_2WO_6 as displayed in Fig. 2g. The d-spacing observed lattice fringe of 0.3084 and 0.2720 nm in Fig. 2h corresponds to the ($\bar{1}$21) crystallographic plane of $BiVO_4$ and the (002) crystallographic plane of the Bi_2WO_6, respectively.

3.3 XPS and ICP analyses

The surface composition and chemical state of Bi_2WO_6, $BiVO_4$, and 2.0 mol% Fe-doped Bi_2WO_6-$BiVO_4$ were identified by X-ray photoelectron spectroscopy (XPS). The spectrum of Bi 4f displayed double peaks located at ~159 and ~164 eV, corresponding to Bi $4f_{7/2}$ and Bi $4f_{5/2}$, respectively, which could be assigned to Bi^{3+} as displayed in Fig. 3a.[24,25] For 2.0 mol%Fe-doped Bi_2WO_6-$BiVO_4$, two peaks ascribed to Bi $4f_{7/2}$ and Bi $4f_{5/2}$ are located at 159.48 eV and 164.78 eV, respectively, which show slightly shifting towards higher binding energy comparing with the pure Bi_2WO_6 (159.38 eV and 164.71 eV) and $BiVO_4$ (158.94 eV and 164.27 eV). This result indicates there is the strong chemical bond generated between $BiVO_4$ and Bi_2WO_6 for forming the composite. Moreover, it should be ascribed to the changing chemical coordination environment of Bi surroundings. This implies that the successful substitution of Fe^{3+} for Bi^{3+} in $BiVO_4$ and Bi_2WO_6. Fig. 3b exhibits the XPS spectra of V 2p orbital in $BiVO_4$ and 2.0 mol% Fe-doped Bi_2WO_6-$BiVO_4$. The V 2p peaks are centered at about 517 eV for V $2p_{3/2}$ and 525 eV for V $2p_{1/2}$, corresponding to V^{5+} in $BiVO_4$.[24,25] The peaks at about 516 eV for V $2p_{3/2}$ and 524 eV for V $2p_{1/2}$ may be ascribed to V^{5+} oxidation state in V_2O_5. The XPS spectra of W 4f display prominent peaks at about 35 eV and 37 eV, corresponding to W $4f_{7/2}$ and W $4f_{5/2}$, respectively, which be ascribed to W^{6+} oxidation state[26,27] in Bi_2WO_6 and 2.0 mol% Fe-doped Bi_2WO_6-$BiVO_4$, as represented in Fig. 3c. The peaks located at 711.28 and 724.96 eV can be assignable to Fe $2p_{3/2}$ and Fe $2p_{1/2}$, orderly, corresponding to Fe^{3+} as shown in Fig.

3d.[28,29] Fig. 3e shows the XPS spectra of O 1s of Bi_2WO_6, $BiVO_4$, and 2.0 mol% Fe-doped Bi_2WO_6-$BiVO_4$. O 1s signal of these samples can be deconvoluted into five main peaks in the range of 529-533 eV. The O 1s main component at about 529-530 eV can be attributed to the lattice oxygen (O^{2-}) of metal oxide semiconductor while small peaks center at about 531-533 eV may be ascribed to the chemisorbed oxygen and hydroxyl species or adsorbed water species from Bi_2WO_6 and $BiVO_4$ particles.[30-32]

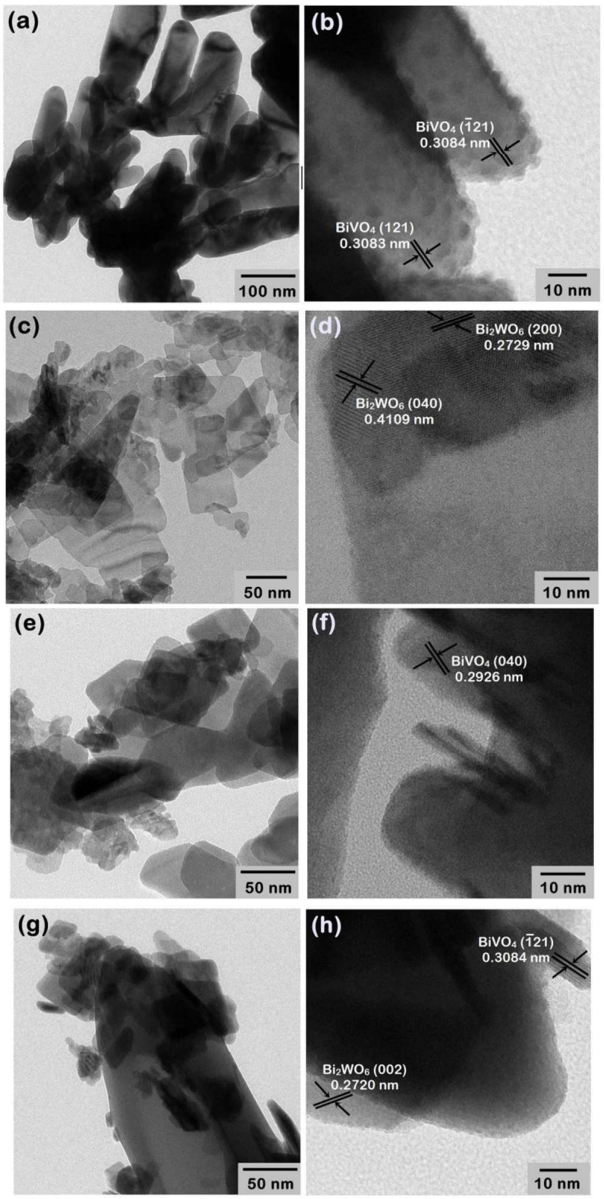

Fig. 2 TEM images and lattice fringes of (a,b) $BiVO_4$, (c,d) Bi_2WO_6, (e,f) Bi_2WO_6-$BiVO_4$ and (g,h) 2.0 mol% Fe-doped Bi_2WO_6-$BiVO_4$ samples.

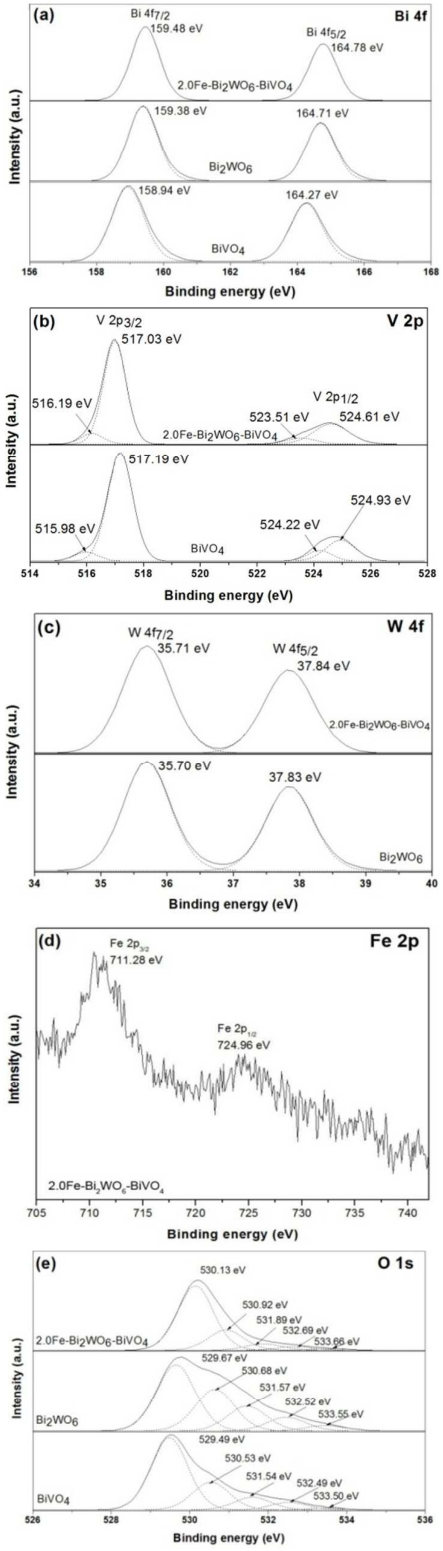

Fig. 3 XPS spectra of (a) Bi 4f, (b) V 2p, (c) W 4f (d) Fe 2p and (e) O 1s of Bi_2WO_6, $BiVO_4$ and 2.0 mol% Fe-doped Bi_2WO_6-$BiVO_4$.

According to the ICP analysis, the iron amount of 0.45, 0.90, 1.90, 4.50 mol% in Bi_2WO_6-$BiVO_4$ composites were investigated from the nominal 0.5, 1.0, 2.0, 5.0 mol% Fe-doped Bi_2WO_6-$BiVO_4$ composite, respectively. This suggests that the degree of Fe doping in the as-synthesized products agrees well with the initial Fe content (0.5-5.0 mol%) and the synthesis process does not lead to significant Fe loss over the investigated compositional range.

3.4 UV-vis DRS analysis

UV-vis diffuse-reflectance spectroscopy (UV-vis DRS) is an important method for characterizing the electronic states and optical properties of semiconductor materials. UV-vis diffuse reflectance spectra of $BiVO_4$, Bi_2WO_6, Bi_2WO_6-$BiVO_4$ and 2.0 mol% Fe-doped Bi_2WO_6-$BiVO_4$ samples were shown in Fig. 4.

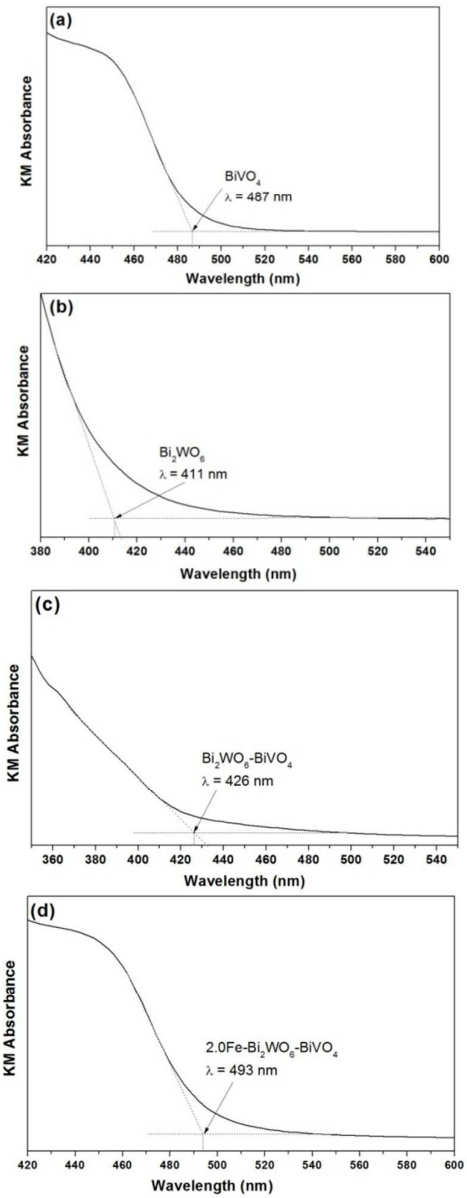

Fig. 4 UV-vis DRS relationship between Kubelka-Munk (KM) absorption versus wavelength of (a) $BiVO_4$, (b) Bi_2WO_6, (c) Bi_2WO_6-$BiVO_4$ and (d) 2.0 mol% Fe-doped Bi_2WO_6-$BiVO_4$ samples.

The absorption spectra can be calculated from the reflectance with Kubelka-Munk (KM) function, as given by the equation: $F(R_\infty) = (1-R_\infty)^2/2R_\infty$, where $F(R_\infty)$ is proportional to the absorption constant of the material, it is indicative of the absorbance of the sample at particular wavelength.[33,34] The samples exhibited an intense absorption in the visible-light range, which suggests the property of being photoactive under visible-light irradiation. The band gap of the samples can be estimated from the equation; $E_g = hc/\lambda$, where E_g is the band gap, h is Planck's constant (6.626×10^{-34} J·s), c is speed of light (2.99×10^8 m/s, and λ is the wavelength. From the band gap calculation, it was found that band gaps of the photocatalysts decrease in the following order:

Bi_2WO_6 (3.02 eV) > Bi_2WO_6-$BiVO_4$ (2.91eV) > $BiVO_4$ (2.55 eV) > 2.0 mol% Fe-Bi_2WO_6-$BiVO_4$ (2.52 eV)

3.5 Photocatalytic activity testing

The photocatalytic activities of all samples were studied via methylene blue degradation under visible-light irradiation. The MB photolysis was found to be 7% under halogen lamp irradiation without photocatalysts. The photocatalytic efficiencies of $BiVO_4$, Bi_2WO_6, Bi_2WO_6-$BiVO_4$, and 0.5, 1.0, 2.0, 5.0 mol% Fe-doped Bi_2WO_6-$BiVO_4$ catalysts were found to be 14%, 17%, 38%, 23%, 21%, 46% and 31%, respectively (Fig. 5a). For comparison, the photocatalytic activity of 2.0 mol% Fe-doped $BiVO_4$ and 2.0 mol% Fe-doped Bi_2WO_6 were evaluated as shown in Fig. S1. The photocatalytic activity of 2.0 mol% Fe-doped Bi_2WO_6-$BiVO_4$ composite is better than that of pure and other doped samples. However, the Bi_2WO_6 reveals the highest specific surface area (44 $m^2\ g^{-1}$) while its photocatalytic property was lower in the photodegradation of methylene blue. This could be ascribed to the photocatalytic performance depending on many factors such as crystallinity, light absorption, and type of catalyst.[35,36] Lower or higher concentration of iron would lead to a decreased the photocatalytic performance. The increment of photocatalytic activity obtained in the case of 2.0 mol% Fe-doped Bi_2WO_6-$BiVO_4$ composite might also be ascribed to Fe ions acting as both electron and hole traps, which enhance the lifetimes of electrons and holes and reduce the e^-/h^+ pair recombination rate.[37-40] Moreover, the mixed phases of monoclinic and tetragonal $BiVO_4$ can be enhanced photocatalytic activity because a spatially separated electron and hole pairs between two distinct phases from the differing potential band levels.[41-43] To further quantitatively comparing the photocatalytic efficiency of all samples, the pseudo-first-order reaction constant was taken using the following equation: $\ln (C_0/C_t) = k_{app}t$, where k_{app} is the apparent pseudo first-order rate constant, C_0 is the initial concentration of dye and C_t is the concentration of dye after irradiation time t.[44] The time-course variation of $\ln(C_0/C_t)$ is exhibited in Fig. 5b. These plots are shown in Fig. 5b, with a good fit observed for the aforementioned model ((R^2) values closing to 1). The pseudo-first-order reaction rate constants of all samples were calculated from the data as shown in Fig. 5c. The k_{app} value of 2.0 mol% Fe-doped Bi_2WO_6-$BiVO_4$ composite provides the highest photocatalytic activity (0.0051 min^{-1}) within 120 min of irradiation.

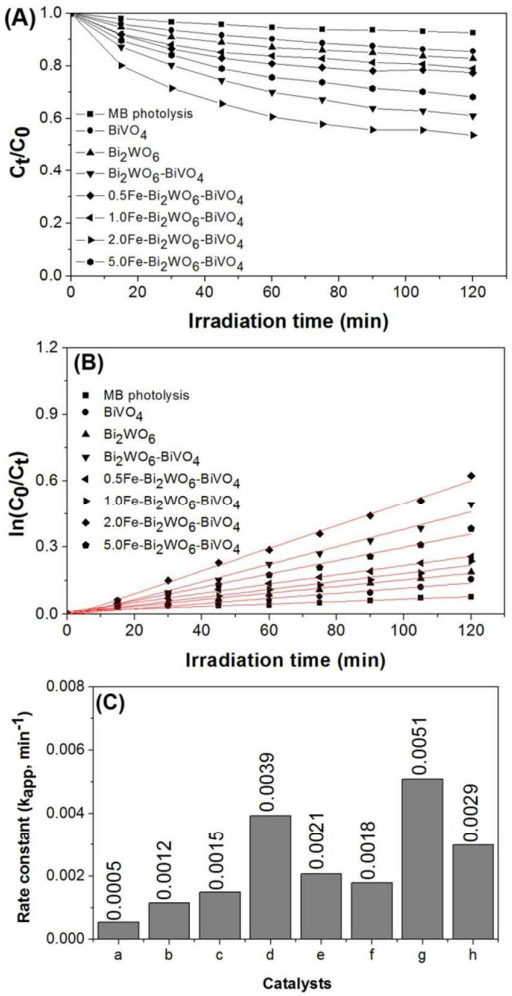

Fig. 5 (A) Photocatalytic activities relationship between C_t/C_0 versus irradiation time and (B) and (C) kinetic plot of apparent association rate constant k_{app} (min^{-1}) of (a) MB photolysis, (b) $BiVO_4$, (c) Bi_2WO_6, (d) Bi_2WO_6-$BiVO_4$, (e) 0.5Fe-Bi_2WO_6-$BiVO_4$, (f) 1.0Fe-Bi_2WO_6-$BiVO_4$, (g) 2.0Fe-Bi_2WO_6-$BiVO_4$, (h) 5.0Fe-Bi_2WO_6-$BiVO_4$ in the degradation of MB under visible light irradiation for 2 h.

To evaluate the stability and reusability of 2.0 mol% Fe-doped Bi_2WO_6-$BiVO_4$ composite, a recycling test was performed as presented in Fig. 6a. The photodegradation of MB was monitored for five cycles (each cycle lasted for 120 min). After 5 times cycling run, the apparent rate constants of the first run to the fifth run are decreased from 0.0051 to 0.0043 min^{-1} (approximate 8%) as shown in Fig. 6b. Therefore, 2.0 mol% Fe-doped Bi_2WO_6-$BiVO_4$ composite is highly stable and does not suffer from the photocorrosion during the photocatalysis processes.

3.6 Photocatalytic mechanism

The proposed photocatalytic mechanism of 2.0 mol% Fe-doped Bi_2WO_6-$BiVO_4$ composite toward the MB degradation under visible light irradiation is shown in Fig. 7. To understand the charge transfer behavior among Fe, Bi_2WO_6, and $BiVO_4$, the band edge positions of the conduction band (CB) and the valence band (VB) of Bi_2WO_6 and $BiVO_4$ samples can be calculated following the equation: $E^0_{CB} = \chi - E^C - 0.5E_g$, where χ is the electronegativity of the semiconductor, E^C is the energy of free electrons on the hydrogen scale of 4.5 eV, and the χ value of $BiVO_4$ and Bi_2WO_6 are 6.03 eV[45] and 6.36 eV[46], respectively. The valence band energy (E_{VB}) can be calculated by following equation: $E_{VB} = E_{CB}+E_g$, where E_{CB} is conduction band energy. The E_g values of about 3.07 eV and 2.54 eV of Bi_2WO_6 and $BiVO_4$, respectively, are evaluated from UV-vis DRS analysis. Based on the band gap positions, the CB and VB edge potentials of Bi_2WO_6 were determined at 0.44 and 3.28 eV, respectively. The CB and VB edge potentials of $BiVO_4$ were at 0.26 and 2.80 eV, respectively.

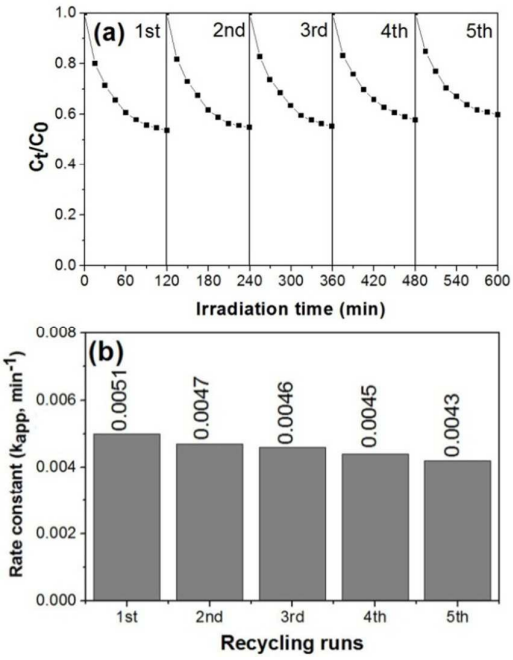

Fig. 6 (a) Recycling runs and (b) rate constants of 2.0 mol% Fe-Bi_2WO_6-$BiVO_4$ sample for MB degradation within 2 h.

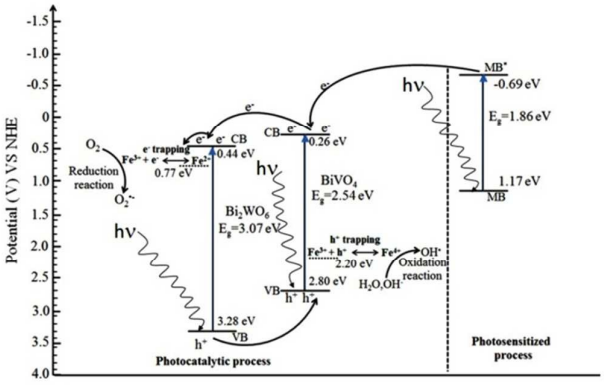

Fig. 7 Photocatalytic mechanism of Fe-doped Bi_2WO_6-$BiVO_4$ composite for the MB degradation under visible light irradiation.

The enhanced photocatalytic processes could also be explained by the increased generation of highly oxidizing hydroxyl radical ($OH^{\bullet}$). As shown in Fig. 7, Fe-doped Bi_2WO_6-$BiVO_4$ composite was excited by visible light irradiation, which induced the generation of electron-hole (e^-/h^+) pairs (Eq. (1)). Under visible light irradiation,

MB molecule 1.17 eV) in aqueous solution can adsorb the visible light to generate the MB* (-0.69 eV) and then inject electrons to CB of $BiVO_4$, and $BiVO_4$ can also be activated by visible light to generate electron and hole pairs. The photoexcited electrons (e^-_{CB}) from $BiVO_4$ will transfer to the conduction band of Bi_2WO_6 catalysts due to the conduction band of $BiVO_4$ is more negative than that of Bi_2WO_6. The electrons will then react with the O_2 surface adsorbates to form superoxide anion radical ($O_2^{\bullet-}$) (Eq. (2). The $O_2^{\bullet-}$ radicals then react with hydroperoxyl radical ($HO_2^{\bullet}$) to produce hydrogen peroxide (H_2O_2), subsequently produce hydroxyl radicals (Eq. (3-5)). These hydroxyl radicals will further oxidize the MB molecules. Following, the photoexcited holes (h^+_{VB}) on the surface of Bi_2WO_6 will react with surface chemisorbed water (H_2O) and hydroxide ion (OH^-) to produce hydroxyl radicals ($OH^{\bullet}$) (Eq. (6-7)). The obtained strong oxidizing agent of hydroxyl radical ($OH^{\bullet}$) can also degrade MB (Eq. (8)). The detailed photodegradation reaction processes are as follows:

$$Fe\text{-}Bi_2WO_6\text{-}BiVO_4 + h\upsilon \rightarrow Fe\text{-}Bi_2WO_6\text{-}BiVO_4\ (h^+_{VB} + e^-_{CB}) \quad (1)$$

Reductive reaction:

$$Fe\text{-}Bi_2WO_6\text{-}BiVO_4\ (e^-_{CB}) + O_2 \rightarrow O_2^{\bullet-} \quad (2)$$

$$O_2^{\bullet-} + MB \rightarrow MB + O_2^{\bullet} \quad (3)$$

$$O_2^{\bullet-} + HO_2^{\bullet} + H^+ \rightarrow H_2O_2 + O_2 \quad (4)$$

$$H_2O_2 \rightarrow 2OH^{\bullet} \quad (5)$$

Oxidative reaction:

$$Fe\text{-}Bi_2WO_6\text{-}BiVO_4\ (h^+_{VB}) + H_2O \rightarrow OH^{\bullet} + H^+ \quad (6)$$

$$Fe\text{-}Bi_2WO_6\text{-}BiVO_4\ (h^+_{VB}) + OH^- \rightarrow OH^{\bullet} \quad (7)$$

$$OH^{\bullet} + MB \rightarrow \text{degradation products} \quad (8)$$

The outcomes of intermediate and final products are important to understand the photocatalytic degradation pathway of methylene blue. This point was illustrated in the work of Houas et al.[47] which detected sulfoxide group, phenolic compound, amino group as the intermediates and sulfate (SO_4^{2-}), nitrate (NO^{3-}), ammonium cation (NH^{4+}), carbon dioxide (CO_2) as the final products of the photocatalytic degradation of methylene blue using titanium dioxide. Huang et al.[48] also found the CO_2 as a final production was produced from MB degradation. Moreover, the photogenerated electron-hole pairs are able to be separated for into trap states in the doped material. The presence of Fe^{3+}, as shown in XPS analysis may act as electron acceptor (from Fe^{3+} to Fe^{2+}) at 0.77 eV and/or hole donor (from Fe^{3+} to Fe^{4+}) at 2.20 eV to facilitate charge carrier localization and hence prolonged separation by trapping at energy levels close to the conduction or valence bands, respectively.[49] Therefore, the Fe^{3+} doping could be effective in producing materials that (1) delay electron-hole recombination, thereby increasing the lifetime of the electron-hole separation[50] as confirmed in PL results and (2) support the charge carrier transfer to the catalyst surface.

The effective charge carrier separation all samples were confirmed by the photoluminescence (PL) technique[51,52] as shown in Fig. 8a. The PL intensity of the 2.0 mol% Fe-doped Bi_2WO_6-$BiVO_4$ composite is lower than that of either pure $BiVO_4$ or Bi_2WO_6 due to lower charges recombination rate. This suggests that the forming composite of these two metal oxides can be enhanced the electron-hole pairs separation.[53,54] Moreover, the photoluminescence spectra for the 2.0 mol% Fe-doped $BiVO_4$ and 2.0 mol% Fe-doped Bi_2WO_6 samples were given for comparing in Fig. S2. The PL intensities of these materials were higher than that of 2.0 mol% Fe-doped Bi_2WO_6-$BiVO_4$ composite. This indicates that the electron and hole pairs can be recombined quickly, resulting in decrease of the photocatalytic activity. However, the 5.0 mol% Fe-doped Bi_2WO_6-$BiVO_4$ composite exhibited the lowest PL intensity but its photocatalytic activity was not the highest value. We attributed this non-consistent of PL and photocatalytic activity to the formation of a recombination center from the excess amount of iron (5.0 mol%) in the composite.[55] To further confirm the effective production of hydroxyl radicals ($OH^{\bullet}$) on the surface of 2.0 mol % Fe-doped Bi_2WO_6-$BiVO_4$ composite was measured via the reaction of terephthalic acid (TA) with $OH^{\bullet}$, and then formed as a fluorescent 2-hydroxy terephthalate (TA-$OH^{\bullet}$) which can be detected by fluorescence spectroscopy[56] as shown in Fig. 8b. The PL intensity of fluorescent 2-hydroxy terephthalate (TA-$OH^{\bullet}$) located at approximated 425 nm and was found that the fluorescence spectra slightly increased with an increasing of irradiation time.

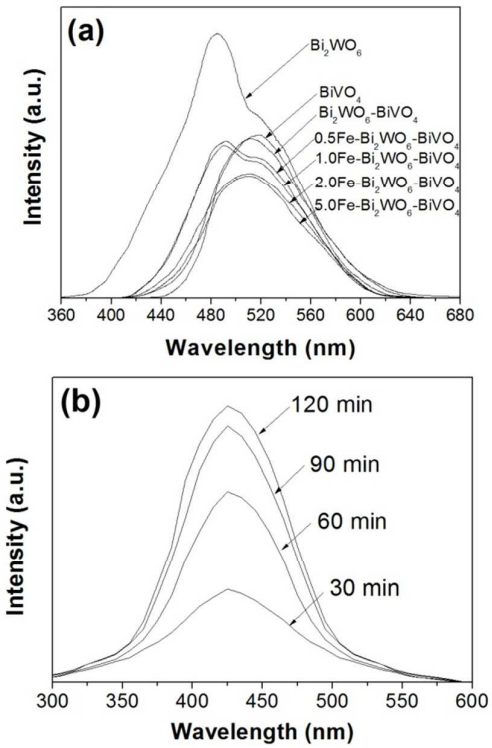

Fig. 8 (a) Photoluminescence (PL) spectra of all samples and (b) fluorescence spectra of a TA-$OH^{\bullet}$ solution generated by 2.0 mol% Fe-Bi_2WO_6-$BiVO_4$ composite under visible light irradiation.

4 Conclusions

Powders made from Bi_2WO_6, $BiVO_4$, Bi_2WO_6-$BiVO_4$, and 0.5-5.0 mol% Fe-doped Bi_2WO_6-$BiVO_4$ particles were successfully prepared by a hydrothermal method. The 2.0 mol% Fe-doped Bi_2WO_6-$BiVO_4$ composite showed the highest photocatalytic activity for degrading of MB under visible light irradiation. This can be attributed to the synergic effects of various factors, such as the excellent crystallinity, amount of iron, charge transfer mechanism, hydroxyl radical production, and strong absorption in the visible light region. The Fe-Bi_2WO_6-$BiVO_4$ composite also showed excellent photostability under visible light and high recyclability for degradation of MB in aqueous solution, implying the possibility of its being used in industrial wastewater treatment in the future.

Acknowledgements

The authors gratefully acknowledge the financial support from the Thailand Graduate Institute of Science and Technology Development Agency (TGIST), National Science and Technology Development Agency (NSTDA); the Thailand Research Fund (TRF) and the higher Education commission (CHE); the National Research University (NRU) Project under the Office of the Higher Education Commission, Ministry of Education, Thailand; Graduate School, the Materials Science Research Center, Department of Physics and Materials Science, Faculty of Science, Chiang Mai University.

References

1 V. Ankita, N. Shamta, Y. Inderjeet and B. Shipra, *Res. J. Chem. Sci.*, 2013, **3(11)**, 60-65.
2 C. Zhang, H. Zhang, K. Zhang, X. Li, Q. Leng and C. Hu, *ACS Appl. Mater. Interfaces*, 2014, **6**, 14423-14432.
3 E. Abdelkader, L. Nadjia and B. Ahmed, *Appl. Surf. Sci.*, 2012, **258**, 5010-5024.
4 B. Zhou, X. Zhao, U. Liu, J. Qu and C.P. Huang, *Appl. Catal. B Environ.*, 2010, **99**, 214-221.
5 T. Wang, C. Li, J. Ji, Y. Wei, P. Zhang, S. Wang, X. Fan and J. Gong, *ACS Sustain. Chem. Eng.*, 2014, **2**, 2253-2258.
6 S. Balachandran, N. Prakash, K. Thirumalai, M. Muruganandham, M. Sillanpää, M. Swaminathan, *Eng. Chem. Res.*, 2014, **53**, 8346−8356.
7 M. Yao, M. Liu, L. Gan, F. Zhao, X. Fan, D. Zhu, Z. Xu, Z. Hao and L. Chen, *Colloid. Surf. A. Physicochem. Eng. Asp.*, 2013, **433**, 132-138.
8 Y. Hu, D. Li, Y. Zheng, W. Chen, Y. He, Y. Shao, X. Fu and G. Xiao, *Appl. Catal. B: Environ.*, 2011, **104**, 30-36.
9 Z. He, Y. Shi, C. Gao, L. Wen, J. Chen and S. Song, *J. Phys. Chem. C.*, 2014, 118, 389-398.
10 N. Wetchakun, S. Chaiwichain, B. Inceesungvorn, K. Pingmuang, S. Phanichphant, A.I. Minett and J. Chen, *ACS Appl. Mater. Interfaces,* 2012, **4**, 3718-3723.
11 L. Li and B. Yan, *J. Alloy. Compd.*, 2009, **476**, 624-628.
12 P. Chatchai, Y. Murakami, S.Y. Kishioka1, A. Y. Nosaka and Y. Nosaka, *Electrochim. Acta.*, 2009, **54**, 1147-1152.
13 N. Tian, Y. Zhang, H. Huang, Y. He and Y. Guo, *J. Phys. Chem. C.*, 2014, **118**, 15640-15648.
14 H. Wang, J. Lu, F. Wang, W. Wei, Y. Chang and S. Dong, *Ceram. Int.*, 2014, **40**, 9077-9086.
15 B. Zhou, X. Zhao, H. Liu, J. Qu and C.P. Huang, *Sep. Purif. Technol.*, 2011, **77**, 275-282.
16 B. Zhou, X. Zhao, H. Liu, J. Qu and C.P. Huang, *Appl. Catal. B: Environ.*, 2010, **99**, 214-221.
17 S. Obregón and G. Colón, *Appl. Catal. B: Environ.*, 2013, **140-141**, 299-305.
18 G. Tan, J. Huang, L. Zhang, H. Ren and A. Xia, *Ceram. Inter.*, 2014, **40**, 1671-11679.
19 A. Zhang and J. Zhang, *J. Hazard. Mater.*, 2010, **173**, 265-272.
20 H. Huang, X. Han, X. Li,S. Wang, P.K. Chu, Y. Zhang, *ACS Appl. Mater. Interfaces*, 2015, **7**, 482-492.
21 P. Pongwan, B. Inceesungvorn, K. Wetchakun, S. Phanichphant and N. Wetchakun, *Eng. J.*, 2012, **16**, 1-10.
22 W. Luo, J. Wang, X. Zhao, Z. Zhao, Z. Lia and Z. Zou, *Phys. Chem. Chem. Phys.*, 2013, **15**, 1006-1013.
23 R.K. Wahi, W.W. Yu, Y. Liu, L. Mejia, J.C. Falkner, W. Nolte and V.L. Colvin, *J. Mol. Catal. A: Chem.*, 2005, **242**, 48-56.
24 P. Cai, S.-M. Zhou, D.-K. Ma, S.-N. Liu, W. Chen and S.-M. Huang, *Micro. Nano. Lett.*, 2015, **7(2)**, 183-193.
25 W.J. Luo, Z.S. Li, Tao Yu and Z.G. Zou, *J. Phys. Chem. C.*, 2012, **116**, 5076-5081.
26 L. Ge and J. Liu, *Appl. Catal. B: Environ.*, 2011, **105**, 289-297.
27 Z. Zhang, W. Wang, E. Gao, M. Shang and J. Xu, *J. Hazard. Mater.*, 2011, **196**, 255-262.
28 X. Wang, Y. Lin, X. Ding and J. Jiang, *J. Alloy. Compd.*, 2011, **509**, 6585-6588.
29 M. Omran, T. Fabritius, A.M. Elmahdy, Nagui A.A. Khalek, M.E. Aref and A.E.H. Elmanawi, *Appl. Surf. Sci.*, 2015, **345**, 127-140.
30 M.S. Gui, W.D. Zhang, Q.X. Su and C.H. Chen, *J. Solid State Chem.*, 2011, **184**, 1977-1982.
31 J. Huang, G.Q. Tan, H.J. Ren, W. Yang, C. Xu, C.C. Zhao and A. Xia, *ACS Appl. Mater. Interfaces*, 2014, **6**, 21041-21050.
32 S. Guo, X.F. Li, H.Q. Wang, F. Dong and Z.B. Wu, *J. Colloid Interface Sci.*, 2012, **369**, 373-380.
33 O. Sacco, V. Vaiano, C. Han, D. Sannino and D.D. Dionysiou, *Appl. Catal. B: Environ.*, 2015, **164**, 462-474.
34 A. Kudo, I. Tsuji and H. Kato, *Chem. Commun.*, 2012, **8(17)**, 1958-1959.
35 N. Getoff, Radiat. *Phys. Chem.*, 2002, **65**, 437-446.
36 K.L. Yeung, S.T. Yau, A.J. Maira, J.M. Coronado, J. Soria and P.L. Yue, *J. Catal.*, 2003, **219**, 107-116.
37 Y. Lin, Z. Jiang, C. Zhu, X. Hu, X. Zhang, H. Zhu, J. Fan and S.H. Lin, *Appl. Catal. B: Environ.*, 2013, **142-143**, 38-44.
38 J.C. Colmenares, M.A. Aramendia, A. Marinas, J.M. Marinas and F.J. Urbano, *Appl. Catal. A: Gen.*, 2003, **306**, 120-127.
39 M.I. Litter, *Appl. Catal. B: Environ.*, 1999, 23, 89-114.
40 U.G. Akpan and B.H. Hameed, *J. Hazard. Mater.*, 2009, **170**, 520-529.
41 S. Obregón, G. Colón, *RSC Adv.*, 2014, **4**, 6920-6926.
42 Z.-F. Huang, L. Pan, J.-Jun Zou, X. Zhang, L. Wang, *Nanoscale*, 2014, **6**, 14044-14063.
43 X. Wang, Q. Xu, M. Li, S. Shen, X. Wang, Y. Wang, Z. Feng, J. Shi, H. Han, C. Li, *Angew. Chem. Int. Ed.*, 2012, **51**, 13089-13092.
44 J. Zhang, H. Cui, B. Wang, C. Li, J. Zhai and Q. Li, *Chem. Eng. J.*, 2013, **223**, 737-746.
45 Y. Xu and M.A.A. Schoonen, *Am. Miner.*, 2000, 85, 543-556.
46 Z.J. Zhang, W.Z. Wang, L. Wang and S.M. Sun, *ACS Appl. Mater. Interfaces*, 2012, **4**, 593-597.
47 A. Houas, H. Lachheb, M. Ksibi, E. Elaloui, C. Guillard, J.-M. Herrmann, *Appl.Catal. B. Environ.*, 2001, **31**, 145-157.
48 Z.-F. Huang, J. Song, L. Pan, X. Jia, Z. Li, J.J. Zou, X. Zhang, L. Wang, *Nanoscale*, 2014,**6(15)**, 8865-8872.
49 T. Masui, H. Hirai and N. Imanaka, *J. Mater. Sci. Lett.*, 2002, **21**, 489-491.
50 Y. Zhang, W. Jiang, C. Wang, F. Namavar, P.D. Edmondson, Z. Zhu, F. Gao, J. Lian and W.J. Weber, *Phys. Rev. B.*, 2010, **82**, 184105-184112.
51 H. Huang, K. Liu, K. Chen, Y. Zhang, Y. Zhang, S. Wang, *J. Phys. Chem. C.*, 2014, **118**, 14379-14387.
52 H. Huang, X. Li, J. Wang, F. Dong, P.K. Chu, T. Zhang, Y. Zhang, *ACS Catal.*, 2015, **5**, 4094-4103.
53 J.J. Sun, X.Y. Li, Q.D. Zhao, J. Ke and D.K. Zhang, *J. Phys. Chem. C.*, 2014, **118**, 10113-10121.
54 Z.-F. Huang, J.-J. Zou, L. Pan, S. Wang, X. Zhang, L. Wang, *Appl. Catal. B. Environ.*, 2014, **147**, 167-174.
55 M.I. Litter, Appl. Catal. B. Environ. 23 (1999) 89-114.
56 Q. Xiang, J. Yu and P.K. Wong, *J. Colloid Interface Sci.*, 2011, **357**, 163-167.

Graphical Abstract